A Novel Accurate Adaptive Constant On-Time Buck Converter for a Wide-Range Operation

Wen-Chin Liu, Ching-Jan Chen, *Senior Member, IEEE*, Ching-Hsiang Cheng, *Student Member, IEEE*, and Hsuan-Ju Chen

***Abstract*—The ripple-based constant on-time (COT) control with ripple compensation has been widely adopted in buck converters in the recent years because of its simplicity, fast transient response, and high light-load efficiency. However, this control has the potential issues of instability and excessive load transient response with wide input/output voltage range conditions in the power management integrated circuit (PMIC) applications. In this article, an accurate adaptive COT control scheme is proposed to solve these problems. The control scheme achieves accurate output voltage, and nearly constant quality factor and well transient response over a wide-range operation with simple circuit. The small-signal model is also derived based on the describing function (DF) technique for design optimization. Finally, the simulations and experimental verifications were conducted to verify the proposed concepts.**

***Index Terms*—Constant on-time (COT), describing function (DF), power management integrated circuit (PMIC), small-signal modeling.**

I. Introduction

In RECENT years, a ripple-based constant on-time (RBCOT) controlled buck converter, as shown in Fig. 1, has been widely applied to the dc–dc conversion and low-end power management integrated circuit (PMIC) applications [1]–[5]. The control scheme has the advantages of simplicity, low cost, fast load transient response, and high conversion efficiency under the light-load conditions. However, due to the omission of the high-gain error amplifier, RBCOT may not meet the output-voltage regulation precision requirements for the CPU V-core applications. Nevertheless, this control is still suitable for many applications such as PMIC to supply I/O power, phase-locked-loop power, and memory power, where the voltage precision is less stringent.

A buck converter with RBCOT control suffers from the subharmonic oscillation instability with ceramic capacitors [1]–[16]. The subharmonic oscillation, as shown in Fig. 2, occurs, while ceramic capacitors with low-equivalent series resistors (ESRs) are implemented as output capacitors. Therefore, numerous ripple compensation schemes have been proposed to enhance the ESR ripple component in a sensed output voltage for stability [1]–[12]. To avoid the subharmonic oscillation issue, one of the schemes is RBCOT with an external ramp compensation. However, in accordance with the articles presented in [2] and [3], the transfer functions of this solution must be factorized to separate poles and zeros, inducing two regions with a relative small ramp and a large ramp compensation. As a result, the external ramp in the RBCOT would cause different behaviors on the control-to-output transfer function under different regions. For large duty cycle operations, the gain peaking of the transfer function would move toward the low frequency and degrade the phase margin significantly. In general, the external ramp

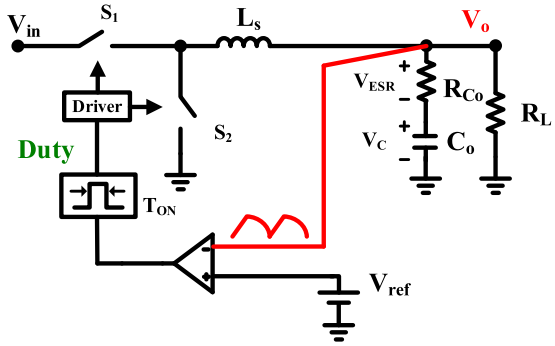

Fig. 1. Circuit diagram of the RBCOT on-time buck converter.

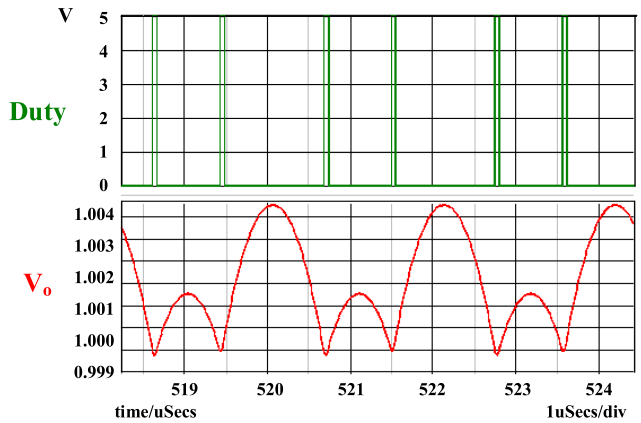

Fig. 2. Time waveform of subharmonic oscillation instability.

Manuscript received January 8, 2019; revised April 18, 2019 and June 20, 2019; accepted August 7, 2019. Date of publication August 20, 2019; date of current version January 10, 2020. This work was supported by a Research Grant from Richtek Corporation to Taiwan University, both in Taiwan, and National Taiwan University under Grant NTU-CC-108L890701. Recommended for publication by Associate Editor L. Corradini. *(Corresponding author: Ching-Jan Chen.)*

W.-C. Liu, C.-J. Chen, and C.-H. Cheng are with the Department of Electrical Engineering, National Taiwan University, Taipei 10617, Taiwan (e-mail: brianliu.pe@gmail.com; chenjim@ntu.edu.tw; wind19871219@gmail.com).

H.-J. Chen is with the Richtek Technology Corporation, Chupei 30288, Taiwan (e-mail: hans_chen@richtek.com).

Color versions of one or more of the figures in this article are available online at http://ieeexplore.ieee.org.

Digital Object Identifier 10.1109/TPEL.2019.2936524

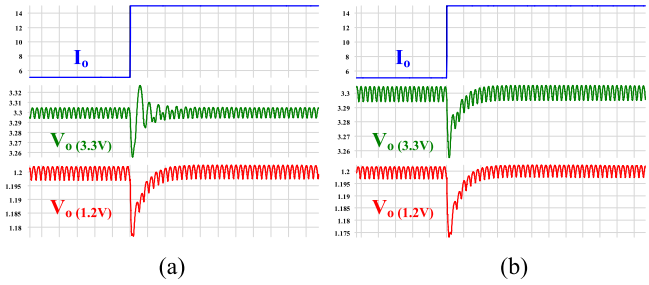

Fig. 3. Transient response with different output voltage for RBCOT control. (a) With fixed slope VIC compensation. (b) With the proposed control.

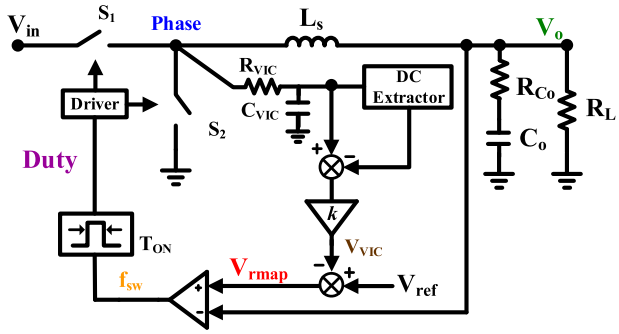

Fig. 4. Circuit diagram of a buck converter with a VIC control scheme.

method is not suitable for wide-range operations with large duty variation since this solution cannot achieve a well-damped performance for ceramic capacitors.

Another control scheme to solve instability was reported by inducing the concept of virtual inductor current (VIC) compensation to RBCOT control [4]–[7]. With this VIC ripple compensation, the control-to-output transfer function is more straightforward to analyze because poles and zeros can readily separate and simplify. Besides, no current sensor is required.

However, the RBCOT control with VIC may not achieve optimal load transient response design under wide-range operations for PMIC applications. Take Intel APL PCIM as an instance [17]. The buck converter must support dynamic voltage scaling, i.e., the output voltage varies from 0.5 to 1.45 V depending on its definition of modes. The output load is from 0 to 20 A. Hence, the output power is from 0 to approximate 30 W. Plus, the input voltage also varies from 5 to 21 V. Under such a wide-range operation, a large ramp compensation is indispensable to avoid instability at worst case. General speaking, in such applications, the fixed ripple compensation cannot be the optimal design under different working conditions since the transfer function varies with different operating points, especially for the quality factor at half switching frequency in the COT schemes. This issue also exhibits in the commercial RBCOT products [8], [11], [12].

Fig. 3 shows the transient response waveforms under the same input voltage but different output voltage conditions for the RBCOT control with VIC and the proposed control, respectively. From Fig. 3(a), it can be observed that the transient response of the output voltage behaves differently under different working conditions since the compensated slope is fixed, which causes quality factor variation with different duty cycle. On the other hand, according to Fig. 3(b), the transient responses are similar to each other because the slope compensation is adaptive to operating points, making the quality factor nearly constant under every operating condition. The detailed mechanism will be illustrated in Section III. As a result, to achieve optimal performances, the compensated slope should adjust automatically according to the variations of working conditions.

In this article, an accurate adaptive constant on-time control (A^2COT) scheme, which adaptively modifies its compensated ripple slope in accordance with the input and output voltage, is proposed. The proposed control shows several advantages such as nearly constant quality factor, well transient response over a wide-range operation, accurate output voltage, and a stable discontinuous conduction mode (DCM) operation. A review of the RBCOT with VIC is discussed in Section II. Later, the circuit diagram and quality factor derivation of the proposed scheme are discussed in Section III. The small-signal model is derived based on a describing function (DF) method in Section IV. Finally, the simulations and experimental results are provided in Section V.

II. Review and Analysis of Buck Converter With VIC

A. Control Law for RBCOT With VIC

RBCOT with VIC, as shown in Fig. 4, is a solution to improve the stability with a ceramic output capacitor [4]. Besides, this control scheme also preserves the advantage of the RBCOT scheme, such as no current sensing circuits. By integrating the phase voltage $V_{\rm phase}$ through an *RC* integrator and a dc exactor, the VIC can be created. The dc extractor consists of a simple *RC* low-pass filter, where the *RC* time constant of the exactor is much higher than the switching frequency to extract the dc value. Then, the VIC waveform is summed with output voltage to enhance the effect of ESR, improving the stability. From the mechanism described above, the rising slope $M_{\rm rise}$ and falling slope $M_{\rm fall}$ of $V_{\rm VIC}$ can be derived separately as follows [4]:

$$M_{\rm rise} = \frac{k\left(V_{\rm in} - V_o\right)}{R_{\rm VIC}C_{\rm VIC}} \tag{1}$$

$$M_{\rm fall} = \frac{kV_o}{R_{\rm VIC}C_{\rm VIC}}. \tag{2}$$

From (1) and (2), it can be observed that the ripple magnitude of VIC is proportional to the steady-state ESR voltage ripple. Thus, the ESR ripple component is effectively enhanced by adding the additional equivalent ripple to the output voltage, making the system more stable.

However, the VIC control scheme has the subharmonic oscillation in a certain DCM condition [7], since, under the DCM condition, there is an interval that both switches are turned OFF. The inductor current equals to zero while the phase voltage would not be zero at this interval. Therefore, there would also be another slope in the sensed VIC ripple during both switches OFF. According to [7], the slope might cause instability. Besides, the output inductor starts resonant with parasitic components at this

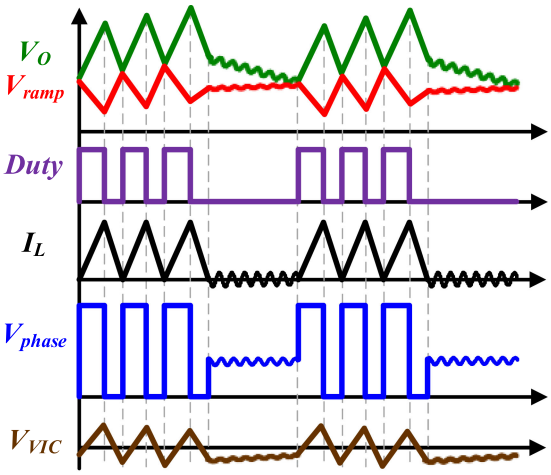

Fig. 5. Unstable waveforms under a DCM operation.

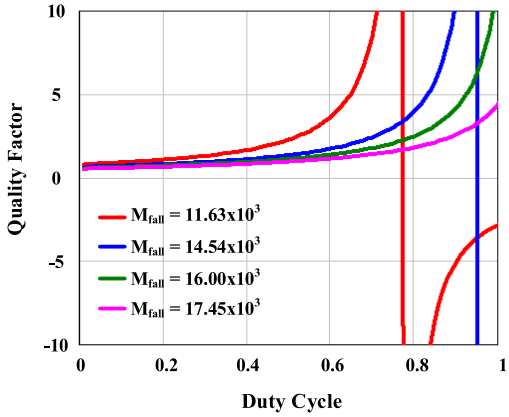

Fig. 6. Quality factor versus duty cycle for different slope compensation.

interval and couple the noisy signals into the VIC. As a result, the noise in the ramp might falsely trigger on-time generator and set duty ON occasionally. The unstable waveforms are shown in Fig. 5. To avoid unstable conditions in the DCM operation, it is indispensable to add extra control circuits, which inevitably increase the complexity of circuit implementation.

B. Small-Signal Model of RBCOT With VIC

To further investigate the small-signal characteristics, the ref-to-output transfer function $G_{vc}(s)$ and output impedance $Z_o(s)$ are derived. $G_{vc}(s)$ can be derived by inserting a small perturbation to $v_{\rm ref}$ and use the DF to obtain the ratio of perturbed output voltage and $v_{\rm ref}$ ($G_{vc}(s) \equiv v_o(s)/v_{\rm ref}(s)$) [5]. With a similar way, the output impedance *Zo(s)* ($Z_o(s) \equiv v_o(s)/i_o(s)$) also can be obtained. According to [5], the expressions are shown by (3) and (4) and the accuracy of these expressions is up to $f_{\rm sw}/2$. Note that k is the VIC gain, and $\tau_{\rm LPF}$ is the time constant of $R_{\rm VIC}$ and $C_{\rm VIC}$. Both $G_{vc}(s)$ and $Z_o(s)$ are the functions of the power-stage parameters (output inductor L_s, output capacitor C_o, and ESR $R_{\rm co}$), working conditions (input voltage $V_{\rm in}$, output voltage V_o, and switching period $T_{\rm sw}$) and the slope of VIC. That is to say, the $G_{vc}(s)$ and $Z_o(s)$, especially their quality factor Q_2, will vary with different operating conditions.

$$G_{vc}(s) \equiv \frac{v_o(s)}{v_{\rm ref}(s)} \approx \frac{R_{C_o}C_o s+1}{\left(1+\frac{s}{Q_1\omega_1}+\frac{s^2}{\omega_1^2}\right)\left(1+\frac{s}{Q_2\omega_2}+\frac{s^2}{\omega_2^2}\right)} \tag{3}$$

$$Z_o(s) \equiv \frac{v_o(s)}{i_o(s)} \approx \left(\frac{R_{C_o}C_o s+1}{\left(1+\frac{s}{Q_1\omega_1}+\frac{s^2}{\omega_1^2}\right)\left(1+\frac{s}{Q_2\omega_2}+\frac{s^2}{\omega_2^2}\right)}-1\right) \times \left(\frac{1}{C_o s}+R_{C_o}\right) \tag{4}$$

where

$$\omega_1 = \pi/T_{\rm on}, \quad Q_1 = 2/\pi$$

$$\omega_2 = \pi/T_{\rm sw}, \quad Q_2 = \frac{T_{sw}}{\pi\left[\left(1+\frac{M_{\rm fall}}{s_f}\right)R_{C_o}C_o - T_{\rm on}/2\right]}$$

$$M_{\rm fall} = \frac{v_{\rm in}kD}{R_{\rm VIC}C_{\rm VIC}}, \quad s_f = \frac{v_{\rm in}D}{L_s}.$$

Fig. 6 illustrates the relationship between the quality factor Q_2, which influences the stability and transient response, and duty cycle with the different VIC slopes. The figure is plotted based on the constant frequency condition where the switching frequency is 750 kHz. The output inductance is 470 nH, output capacitance is 90 μF, ESR is 0.28 mΩ. From the figure, it can be observed that the quality factor varies with the duty cycle variation. Moreover, if the VIC slope is insufficient, the quality factor may turn out to be a negative value, which causes an unstable situation, such as red and blue lines. Even though sufficient slope compensation can make a sure stable operation, such as a purple line, the quality factor still varies with different duty cycle, causing different transient response performance. According to output impedance $Z_o(s)$, under the wide range operating conditions, the variation of quality factor may cause different ringing phenomenon at the output voltage. For dynamic load transient response, the overshoot/undershoot of output voltage is extremely critical to some dc–dc conversion applications such as the V-core applications which may change load current periodically. Therefore, the quality factor design is very pivotal.

III. Proposed A^{2}COT

Fig. 7 shows the circuit diagram of A^{2}COT for the buck converter. This control scheme contains two feedback loops. The inner loop directly feedbacks the output voltage signal, which enhances the transient response. The outer loop consists of a compensator and adaptive ramp generator, which regulate output voltage, ensure stability, and similar transient response at a wide operation range. The ramp generator is made up of a high-side transconductor, which is controlled by the compensator output V_c, and a low-side transconductor, which is controlled by the

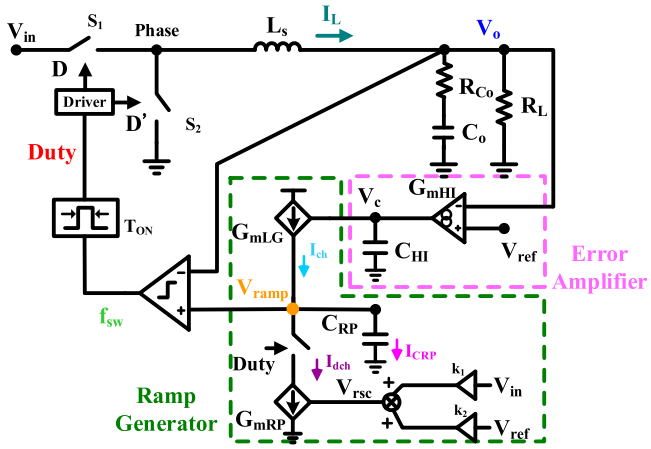

Fig. 7. Circuit diagram of A^{2}COT for a buck converter.

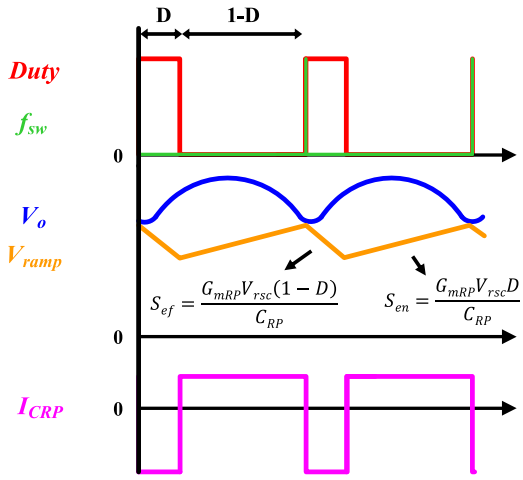

Fig. 8. Modulation waveforms for A^{2}COT.

ramp slope control voltage $V_{\rm rsc}$. The function of the ramp slope control voltage $V_{\rm rsc}$ is used to achieve near constant quality factor, which will be introduced in the next section and it is a combination of different weighting of the input voltage and the reference voltage.

The detail modulation waveforms are demonstrated in Fig. 8. When the high-side switch of the buck converter turns OFF, the low-side transconductor would also be cut OFF. The high-side transconductor charges the ramp capacitor $C_{\rm RP}$ until the ramp voltage $V_{\rm ramp}$ equals to the output voltage $V_{\rm o}$, which triggers the high-side switch of the buck converter to turn ON. Then, when the high-side switch of the buck converter turns ON, the low-side transconductor discharges the ramp capacitor $C_{\rm RP}$ for a period equals to on-time. Therefore, unlike the external ramp, the VIC scheme, and the other enhanced V^{2}COT schemes, this control scheme generates a ripple signal without the adder. In other words, the proposed control scheme generates inverse ramp and add to reference voltage automatically rather than uses an adder to inverse the ramp and add to reference voltage. Moreover, this control scheme can regulate output voltage accurately owing to the high gain compensator $G_{\rm mHI}$ and $C_{\rm HI}$ inserted.

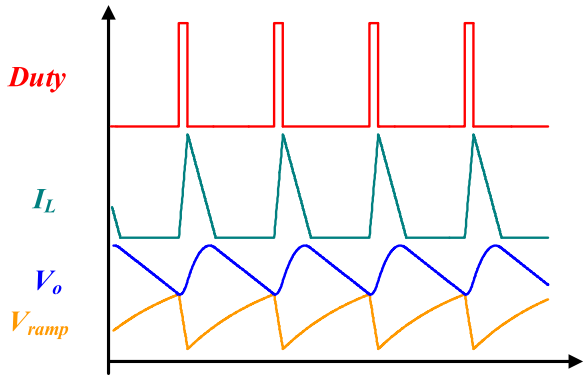

Fig. 9. DCM operation waveforms.

From Fig. 8, the rising slope S_{en} and the falling slope S_{ef} of $V_{\rm ramp}$ can be obtained as (5) and (6) by the steady-state ampere-second balance calculation of the ramp capacitor $C_{\rm RP}$. The detail derivation is shown in the appendix. Unlike the external ramp which resets to zero each cycle, the $V_{\rm ramp}$ is a continuous ripple and is proportional to the inductor current ripple. Therefore, the modulation scheme is classified as VIC

$$S_{en} = \frac{G_{\rm mRP} V_{\rm rsc} D}{C_{\rm RP}} \tag{5}$$

$$S_{ef} = \frac{G_{\rm mRP} V_{\rm rsc}\,(1-D)}{C_{\rm RP}}. \tag{6}$$

Fig. 9 shows the detail DCM waveforms of the proposed scheme. When the load decreases, the switching frequency decreases correspondingly. Since the low-side current discharge the ramp capacitor $C_{\rm RP}$ with a fixed charge, the average value of the high-side current would be lower for a longer off-time. The modulation law would be similar to the continuous conduction mode (CCM) mode as shown in Fig. 9. In this control, unlike the VIC control scheme, there is no stability issue in the DCM operation since this control scheme does not possess the third slope when inductor current equals to zero and both switches of the buck converter are turned OFF.

IV. Small-Signal Model Derivation of A^{2}COT Control

In this section, a small-signal model and stability criteria are derived for the proposed A^{2}COT control. The DF method [2], [5], [10] is used for accurately modeling because this approach preserved the ripple-frequency components during derivation. Hence, the accuracy of the model is up to the half of switching frequency.

A. Control-to-Output Transfer Function

According to the DF method, the small-signal model of the A^{2}COT control was developed. First of all, a small sinusoidal voltage with perturbed frequency f_m is inserted to control voltage V_c, as shown in Fig. 10. Then, the duty cycle will be modulated by the perturbation accordingly. With the Fourier analysis, control to duty transfer function can be derived by

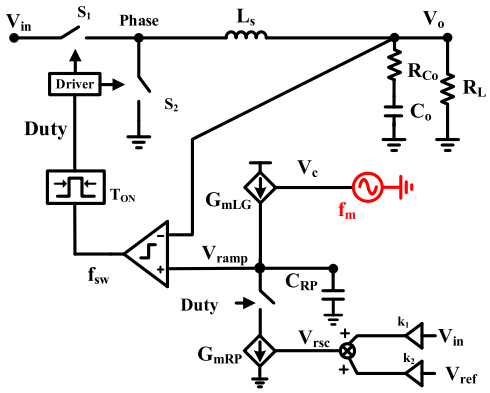

Fig. 10. Modeling methodology for control-to-output transfer function.

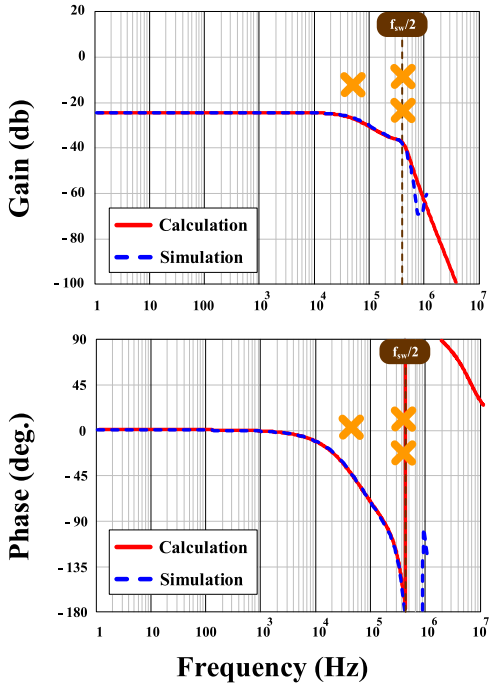

Fig. 11. Model verification of control-to-output transfer function. (Dotted line: SIMPLIS simulation, solid line: calculation).

calculating the perturbed magnitude [2], [5], [10]. The detailed derivation is illustrated in the Appendix.

The derived control-to-output transfer function can be simplified as follows using Padé approximation:

$$\frac{v_o(s)}{v_C(s)} \approx \frac{G_{\mathrm{mLg}}R_{\mathrm{eq}}}{1+sC_{\mathrm{RP}}R_{\mathrm{eq}}} \frac{R_{Co}Cs+1}{1+\frac{s}{Q_1\omega_1}+\frac{s^2}{\omega_1^2}} \frac{1}{1+\frac{s}{Q_2\omega_2}+\frac{s^2}{\omega_2^2}} \quad (7)$$

where

$$\omega_1 = \pi/T_{\mathrm{on}}\ ,\quad Q_1 = 2/\pi\ ,\quad \omega_2 = \pi/T_{\mathrm{sw}}$$

$$Q_2 = \frac{T_{\mathrm{sw}}}{\pi\left[\left(1+\frac{s_{en}}{s_f}\right)R_{C_o}C_o - T_{\mathrm{on}}/2\right]}$$

$$s_{en} = \frac{G_{\mathrm{mRP}}V_{\mathrm{rsc}}D}{C_{\mathrm{RP}}}\ ,\quad s_f = \frac{v_{\mathrm{in}}D}{L_s}$$

$$R_{\mathrm{eq}} = \frac{V_{\mathrm{ref}}}{G_{\mathrm{mRP}}V_{\mathrm{rsc}}D}.$$

S_f represents the falling slope of the inductor current.

From (7), it can be observed that there is a low-frequency pole related to the network of charging and discharging ramp capacitor C_{RP}. In addition to the low-frequency pole, there are the two pairs of high-frequency pole and the locations are at half switching frequency and twice on-time period, respectively, which are related to the direct voltage feedback loop [13], [14]. Due to the Padé approximation, the accuracy of this small-signal model is up to half switching frequency. The simulated and calculated transfer functions are matched as shown in Fig. 11, where input voltage is 19 V_{dc}, output voltage is 1.2 V_{dc}, and switching frequency is 750 kHz.

The stability criteria can be derived from the quality factor Q_2 at half-switching frequency, which is related to the ratio of slope of ramps. In order to ensure the stable operation, the internal ramp needs to make sure that Q_2 is positive. That is, $(1+s_{en}/s_f)R_{Co}C_o$ should be larger than $T_{\mathrm{on}}/2$. Another intriguing thing is that the quality factor in (7) is the same as the quality factor in (3). Therefore, the variation of the quality factor at half-switching frequency is shown in Fig. 14, which is determined by the proportion of input and reference voltage. The detail explanation will be illustrated in next section.

To obtain a more accurate stability criterion, it is necessary to take delay time into consideration. Thus, delay time effect was taken into consideration in the derivation for more accurate criterion [5]. The delay time is defined as the time period between the instant of a pulsewidth modulation input intersection and high-side switch turning ON. The derivation result of the quality factor Q_2' at half switching frequency is obtained in (8), where T_d represents the delay time. According to (8), the delay time will deteriorate the stability criterion. Hence, the effect of time delay is very critical for the system, especially for small on-time

$$Q_2'' = \frac{T_{\mathrm{sw}}}{\pi\left[\left(1+\frac{s_{en}}{s_f}\right)R_{C_o}C_o - \left(\frac{T_{\mathrm{on}}}{2}+T_d\right)\right]}. \quad (8)$$

$$Z_o(s) = \frac{C_{\mathrm{RP}}R_{\mathrm{eq}}s}{1+sC_{\mathrm{RP}}R_{\mathrm{eq}}}\left(R_{Co}+\frac{1}{C_o s}\right)\left(\frac{f_s}{s}\frac{V_{\mathrm{in}}}{L_s}\frac{1}{S_f+S_{en}}\frac{\left(1-e^{-sT_{\mathrm{on}}}\right)\left(1-e^{-sT_{\mathrm{sw}}}\right)}{\left(1+\frac{S_f}{S_f+S_{en}}\frac{T_{\mathrm{off}}}{2R_{Co}C}\right)-\left(1-\frac{S_f}{S_f+S_{en}}\frac{2T_{\mathrm{on}}+T_{\mathrm{off}}}{2R_{Co}C_o}\right)e^{-sT_{\mathrm{sw}}}}-1\right) \quad (9)$$

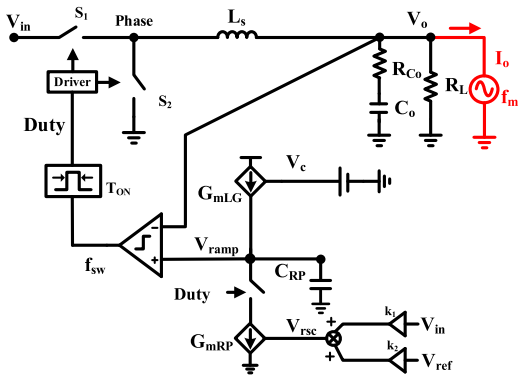

Fig. 12. Modeling methodology for output impedance.

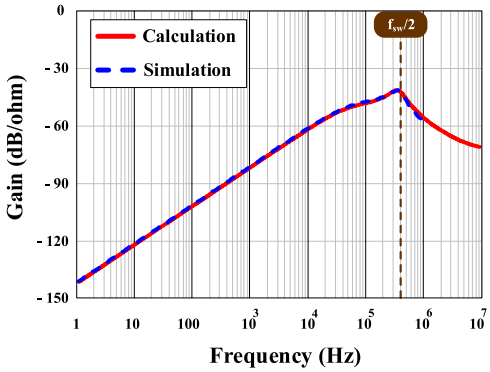

Fig. 13. Model verification of output impedance with open outerloop. (Dotted line: SIMPLIS simulation, solid line: calculation).

B. Output Impedance Transfer Function

The output impedance can also be derived on the basis of similar methodology. Fig. 12 shows the sinusoidal perturbation with a small magnitude at perturbed frequency f_m, injected to system's output. Then, in accordance with the perturbed waveforms, the transfer function from output current to output voltage can be obtained through the mathematical derivation of DF. In the derivation, the outer loop is opened by removing compensator and connecting to a fixed voltage. The inner loop of direct output voltage feedback is kept close. In the s-domain, the output impedance is derived as follows.

(9) shown at the bottom of the previous page, can be simplified by the Padé approximation, and the simplified output impedance is expressed as follows:

$$Z_o(s) \approx \frac{C_{\mathrm{RP}} R_{\mathrm{eq}} s}{1 + s C_{\mathrm{RP}} R_{\mathrm{eq}}} \times \left(\frac{R_{Co} C s + 1}{1 + \frac{s}{Q_1 \omega_1} + \frac{s^2}{\omega_1^2}} \frac{1}{1 + \frac{s}{Q_2 \omega_2} + \frac{s^2}{\omega_2^2}} - 1 \right) \left(R_{Co} + \frac{1}{C_o s} \right). \tag{10}$$

Fig. 13 shows the output impedance with open outer loop by calculation and simulation separately, where input voltage is 19 V_{dc}, output voltage is 1.2 V_{dc}, and switching is 750 kHz. The output impedance is ultralow throughout the wide frequency range since the load current information is sensed [13], [14]. Besides, there is a compensator composed of G_{mHI} and C_{HI} in the system, which could further reduce closed-loop output impedance. Therefore, this control scheme can achieve a fast load transient response.

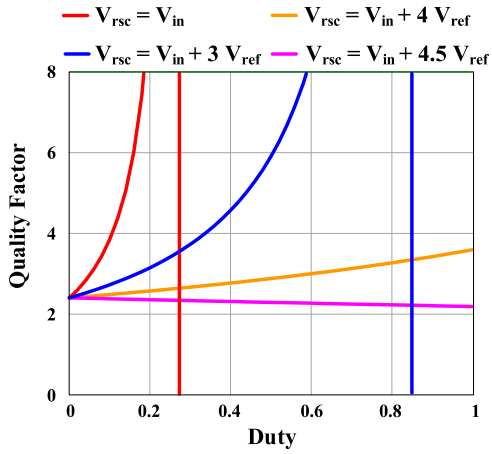

Fig. 14. Quality factor versus duty cycle with different ramp slope control voltage (V_{rsc}).

C. Proposed Invariant Qualify Factor Function at a Wide Operation Range

As mentioned in Section II, the quality factor Q_2 is crucial for the system stability and transient response. An invariant quality factor is preferred to ensure stability and proper transient response at a wide operation range. According to the small-signal derivation results in (7), the quality factor Q_2 is related to the slope of ramp compensation and inductor current, output capacitance, ESR, on-time and switching period. In these variables, the ramp slope *Sen* is the only adjustable variable while others are determined initially. Moreover, based on (5), the slope of the ramp compensation S_{en} is related to the duty cycle D, ramp capacitor C_{RP}, transconductance G_{mRP}, and ramp slope control voltage V_{rsc}. Once again, the only adjustable parameter is ramp slope control voltage V_{rsc}. As a result, the V_{rsc} can be designed deliberately to achieve the invariant quality factor.

The plot of the relationship between the quality factor and duty cycle with different ramp slope control is shown in Fig. 14, where switching frequency is 120 kHz. It is worth to mention that switching frequency is kept constant under different input and output voltages by widely used adaptive on-time control [11], [12]. It can be observed that if the ramp control voltage V_{rsc} is equal to the input voltage, the tendency of quality factor variation is similar to VIC, which is the red line plotted in Fig. 14. On the other hand, it is interesting that if the V_{rsc} is equal to the reference voltage, the tendency is totally inverse, comparing to the input voltage case. Because of this intriguing phenomenon, the V_{rsc} can be set as the combination of the input voltage and reference voltage in order to cancel each other's effect. The orange and purple line in Fig. 14 are plotted for different V_{rsc}, which consists of input voltage and reference voltage with different weighting. It is obvious that the variation of the quality

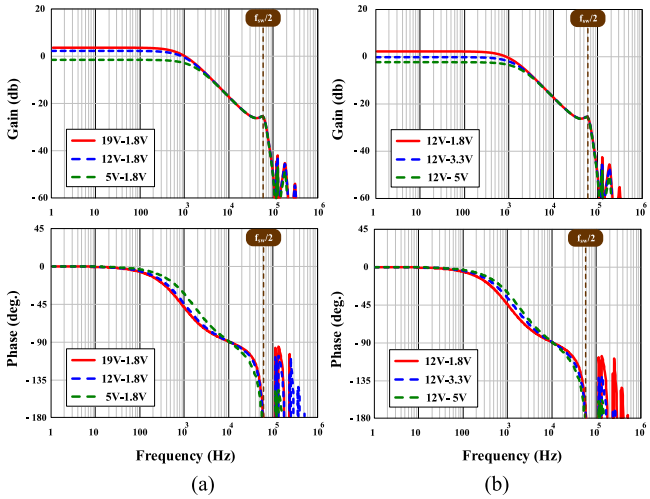

Fig. 15. Control-to-output transfer function verification with different working conditions. (a) Different input voltage. (b) Different output voltage.

factor can be narrowed down significantly with weighted voltage components because $V_{\rm rsc}$ varies corresponding to the different operating conditions, such as the input voltage and the output voltage.

As for the initial quality factor value, it can be obtained by setting the duty approaches zero in Q_2 equation shown in (7). There are a few variables affecting initial Q value including switching period, the slope of the inductor current, the slope of the ramp, and output RC time constant. Therefore, the Q_2 can be deliberately designed to achieve a well-damped system as well as maintain its invariant Q benefits.

V. Simulation and Experimental Verifications

A. Simulation Verifications

To verify the invariant quality factor function, the SIMPLIS software simulation is used, where its accuracy is widely proved [2]–[7]. Fig. 15 shows the simulation results of the control to output transfer function bode plots under different operating conditions. Form the plots, the gain peaks at half-switching frequency perfectly overlap with each other. That is to say, the quality factors are almost constant under different operating conditions. From simulations, the constant quality factor function of the proposed scheme had been verified.

B. Experimental Verifications

1) Circuit Implementation and Modulation Waveforms: To verify the proposed control, a buck converter with the A^{2}COT control scheme had been implemented by the discrete components. Fig. 16 shows the prototype of the proposed control scheme and the experimental platform. The experimental parameters of the circuit are listed in Table I. The switching frequency operates at 120 kHz due to the limitation of the discrete components time delays.

According to Table I, the quality factor variations with the different $V_{\rm rsc}$ voltage are plotted in Fig. 17. To achieve nearly

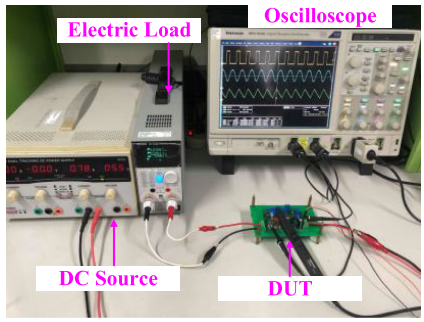

Fig. 16. Experimental platform for the proposed control scheme.

TABLE I
Experimental Parameters

Parameters	Values
Input voltage V_{in} range	5-19 V
Output voltage V_o range	1.8 – 3.3 V
Output current I_o range	0-10 A
Maximum output power P_o	33 W
Switching frequency	120 kHz
Output inductor L_s	3.3 µH
Output capacitor C_o	73 µF
ESR of output capacitor R_{Co}	4.64 mΩ
High-side transconductance G_{mLG}	418 µA/V
Low-side transconductance G_{mRP}	220 µA/V
Ramp capacitor C_{RP}	49 nF
Ramp slope control voltage V_{rsc}	V_{in} + 4.5V_{ref}

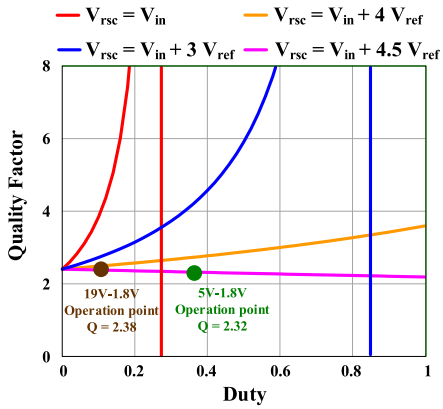

Fig. 17. Quality factor variations with different ramp slope control voltage ($V_{\rm rsc}$) for Table I.

constant quality factor for a wide-range operation, the ramp slope control voltage $V_{\rm rsc}$ finally selected to be $V_{\rm in} + 4.5\ V_{\rm ref}$.

The CCM and DCM modulation waveforms are shown in Fig. 18(a) and (b), respectively. The input voltage is 5 V, the output voltage is 1.8 V, and the operating frequency is 120 kHz. When the ramp voltage is larger than the output voltage, the duty would be triggered and set to a high level. From the experimental results, the output voltage can be regulated to 1.8 $V_{\rm dc}$ accurately. Stable operation is also achieved in DCM.

2) Small-Signal Model With Different Input Voltage: To examine the constant quality factor concept and the proposed small-signal models, the bode plots of control-to-output transfer

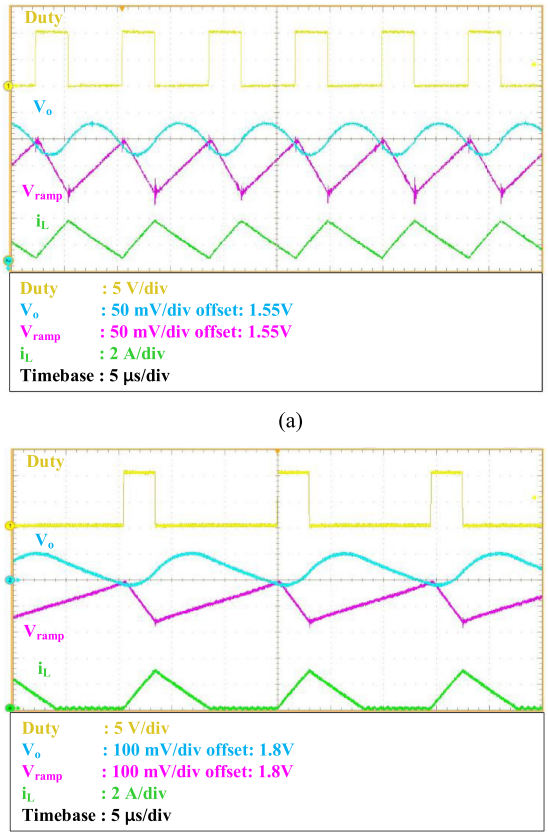

Fig. 18. Experimental modulation waveforms for a 5 to 1.8 V condition. (a) CCM. (b) DCM.

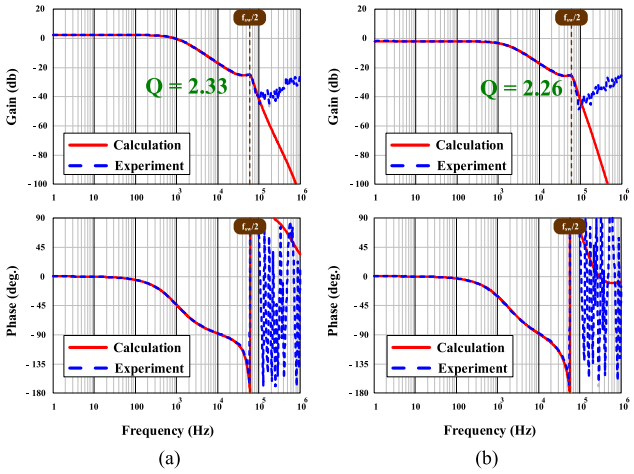

Fig. 19. Control-to-output transfer function verifications of the proposed control scheme. (a) 19 to 1.8 V condition. (b) 5 to 1.8 V condition.

function with different working conditions are measured based on the designed parameters in Table I. Fig. 19(a) and (b) shows the bode plots that inputs 19 and 5 V, separately. From the figures, it can be observed that the quality factor for the different operating conditions are 2.33 for 19 V input voltage and 2.26 for

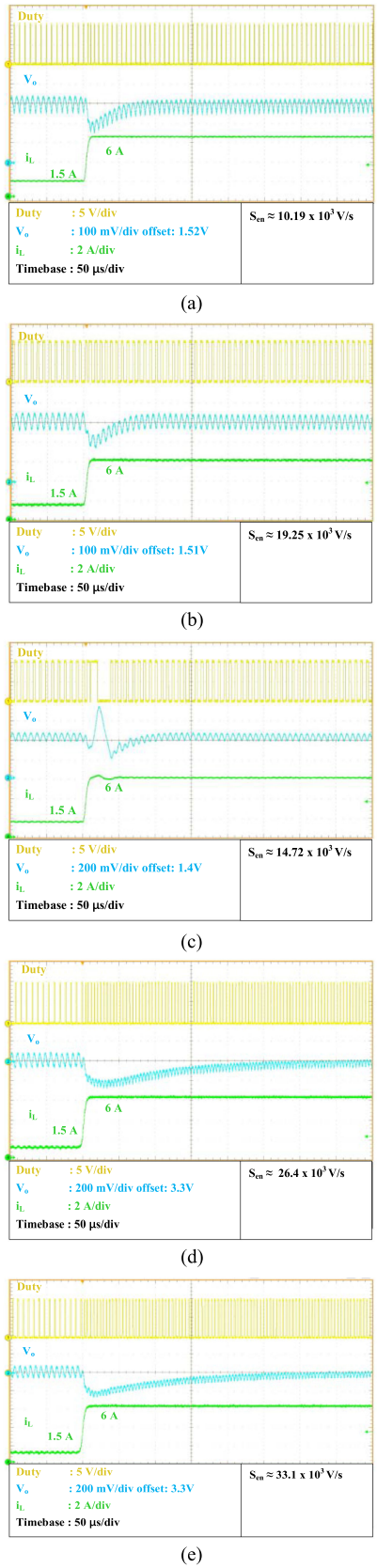

Fig. 20. Load transient response comparison. (a) 19 to 1.8 V. (b) 5 to 1.8 V with the proposed constant Q function. (c) 5 to 1.8 V without the constant Q function. (d) 19 to 3.3 V with the constant Q function. (e) 12 to 3.3 V with the constant Q function.

5 V input voltage. The quality factors match the expected quality factors shown in Fig. 17 where the expected quality factors are 2.38 and 2.32 for 19 and 5 V, respectively. Besides, the bode plots of calculation and experiment perfectly fit each other in both working conditions before half switching frequency.

3) Load Transient Response Comparison: Another benefit of constant quality factor is the better transient response under the wide-range operations. As mentioned in the introduction, with nonadaptive slope compensation, different working conditions would result in different transfer functions and quality factors. As a result, the transient response would be different obviously. On the other hand, with adaptive slope compensation, the transient response would be improved significantly. Fig. 20(a) shows the transient response from 1.5 to 6 A with 1 A/μs slew rate under 19 V input voltage and 1.8 V output voltage condition. Fig. 20(b) shows the same load transient response with the proposed constant quality factor design under the 5 V input voltage and 1.8 V output voltage condition. Fig. 20(c) shows the load transient response without constant quality factor design under the 5 V input voltage and 1.8 V output voltage condition. In Fig. 20(c), the quality versus duty cycle line is selected as $V_{\rm in}$ + 3 $V_{\rm ref}$, whose quality factor has a large variation. All of them use the same compensator, that crossover frequency is selected as 10 kHz. The S_{en} represents the rising slope of ramp compensation. In this comparison, the quality factor for Fig. 20(a) is 2.38, for Fig. 20(b) is 2.32, which is quite close. On the other hand, the quality factor for Fig. 20(c) is around 4.38. This can explain why the adaptive control with constant Q achieve the similar transient response at different condition, while nonadaptive control exhibits large overshoot in the transient response. According to the comparison, it is obvious that the adaptive ramp is very essential for the converters operating under the wide-range conditions.

The different output voltage conditions are also shown in Fig. 20(d) and (e), which are 19 to 3.3 V and 12 to 3.3 V, respectively. The quality factors for these two conditions are also similar to each other as 2.36 and 2.34, separately.

VI. Conclusion

In this article, the ripple-based control with VIC is reviewed initially. Then, a novel adaptive ramp control scheme is proposed to improve the stability and performance under DCM and a wide-range operation. The proposed scheme uses the input and output voltage with different weighting to adjust the slope compensation, achieving near constant quality factor and load transient response under the wide range operation. The control-to-output transfer function and output impedance including delay time effect also had been derived and verified. Finally, a prototype was implemented for verification. The proposed control scheme is very suitable for the PMIC applications with the wide dynamic operating conditions.

Appendix

A. Ramp Slope Derivation for a A^2COT Control Scheme

The ramp generation circuit, as shown in Fig. 21, can be separated into the two operation modes, ON-time and OFF-time

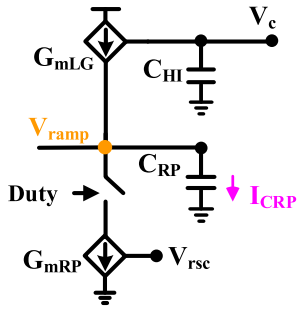

Fig. 21. Ramp generation circuit.

modes. Therefore, it can be expressed by the two equations for ON and OFF separately. During ON-time period, the low-side voltage controlled current source would discharge the ramp capacitor $C_{\rm RP}$ and can be expressed as (11). On the other hand, during the OFF-time period, the low-side current source would be turned OFF, and the high-side current source would start to charge the ramp capacitor $C_{\rm RP}$, which can be expressed as (12)

$$I_{\rm CRP(D)} = G_{\rm mLg}V_c - G_{\rm mRP}V_{\rm rsc} \tag{11}$$

$$I_{\rm CRP(1-D)} = G_{\rm mLg}V_c. \tag{12}$$

Then, according to the ampere-second balance, it can be assumed that the charge of ramp capacitor $C_{\rm RP}$ is balanced under a steady-state operation. Consequently, charge balance can be expressed as follows by (11) and (12):

$$\frac{T_{sw}}{C_{\rm RP}}\left[I_{\rm CRP1}\cdot D + I_{\rm CRP2}\cdot(1-D)\right] = 0. \tag{13}$$

Substituting (11) and (12) into (13), the equation can be simplified as follows:

$$G_{\rm mLg}V_c = G_{\rm mRP}V_{\rm rsc}D. \tag{14}$$

In accordance to the definition of slope, the rising slope and falling slope can be defined as follows:

$$S_{en} = \frac{G_{\rm mLg}V_c}{C_{\rm RP}} \tag{15}$$

$$S_{ef} = \frac{1}{C_{\rm RP}}\left(G_{\rm mRP}V_{\rm rsc} - G_{\rm mLg}V_c\right). \tag{16}$$

Then, the expression of slopes can be further simplified by substituting (14) into (15) and (16). Finally, the slopes can be express as follows:

$$S_{en} = \frac{G_{\rm mRP}V_{\rm rsc}D}{C_{\rm RP}} \tag{17}$$

$$S_{ef} = \frac{G_{\rm mRP}V_{\rm rsc}\left(1-D\right)}{C_{\rm RP}}. \tag{18}$$

B. Control-to-Output Transfer Function Derivation

Step 1: Model assumption

To simplify the complexity of the Fourier analysis, several assumptions were postulated. 1) Slopes of the inductor current and ramp remain constant during ON-time and OFF-time period. 2) Amplitude of perturbation is much smaller than the perturbed

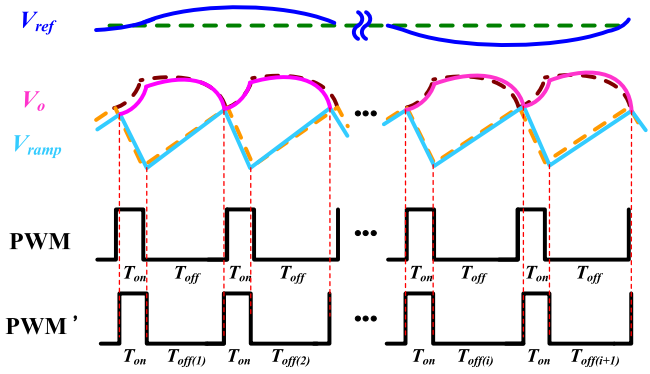

Fig. 22. Modulation waveforms with perturbation for the proposed control.

voltage, such as $V_{\rm ref}$. 3) Switching frequency f_s and perturbation frequency f_m are commensurable.

Step 2: OFF-time calculation from the time waveforms

When a perturbation V_c is applied for modeling, the modulation waveforms under the CCM operation are shown in Fig. 22. Perturbation V_c can be expressed by (19). The modulation with perturbation can be derived from the amp-balance of ramp capacitor $C_{\rm RP}$ and shown in (20). The OFF-time can be obtained from (19) and (20) where $T_{\rm off(i)} = T_{\rm off} + \Delta T_{\rm off(i)}$ and $\Delta T_{\rm off(i)}$ is the delta OFF-time of the ith cycle with perturbation. Finally, the delta OFF-time $\Delta T_{\rm off(i)}$ can be derived as (21) shown at the bottom of this page, where $s_f = R_{\rm Co}V_o/L_s$, and $R_{\rm eq} = V_{\rm ref}/(G_{\rm mRP}V_{\rm rsc}{\rm D})$

$$v_c(t) = r_o + \hat{r}\sin(2\pi f_m t), \quad \hat{r} \ll r_o \tag{19}$$

$$\begin{aligned} &V_{\rm ramp}(t_{i-1} + t_{{\rm off}(i-1)}) \\ &- \int_{t_{i-1}+T_{{\rm off}(i-1)}}^{t_i} \frac{[i_L(t) - v_o(t)/R_L]}{C_o} \cdot dt \\ &= V_{\rm ramp}(t_i + t_{{\rm off}(i)}). \end{aligned} \tag{20}$$

Step 3: Fourier analysis of an inductor current

The perturbed duty cycle and perturbed inductor current can be expressed as follows:

$$\begin{aligned} &d(t)|_{0\le t\le t_M+T_{{\rm off}(M)}+T_{\rm on}} \\ &= \sum_{i=1}^{M}\left[u\left(t - t_i - T_{{\rm off}(i)}\right) - u\left(t - t_i - T_{{\rm off}(i)} - T_{\rm on}\right)\right] \end{aligned} \tag{22}$$

$$\begin{aligned} &i_L(t)|_{0\le t\le t_M+T_{{\rm off}(M)}+T_{\rm on}} \\ &= \int_0^t \left[\frac{V_{\rm in}}{L_s} d(t)|_{0\le t\le t_M+T_{{\rm off}(M)}+T_{on}} - \frac{V_o}{L_s}\right] dt + i_{Lo}. \end{aligned} \tag{23}$$

Then, the Fourier analysis can be used to derive the Fourier coefficient C_m at the perturbation frequency f_m. By substituting (22) into (23), the Fourier coefficient C_m of the inductor current is derived as follows:

$$\begin{aligned} c_{m(i_L)} &= j\frac{2f_m}{N}\int_0^{t_M+T_{{\rm off}(M)}+T_{on}} i_L(T)\, e^{-j2\pi f_m t} dt \\ &= \frac{1}{N\pi}\frac{V_{\rm in}}{L_s} e^{-j2\pi f_m T_{\rm off}}\left(e^{-j2\pi f_m T_{\rm on}} - 1\right) \\ &\quad \times \left[\sum_{i=1}^{M}\left(e^{-j2\pi f_m (i-1)T_{sw}} \sum_{k=1}^{i}\Delta T_{{\rm off}(k)}\right)\right]. \end{aligned} \tag{24}$$

Step 4: DF derivation

By substituting (21) into (23), the transfer function from V_c to inductor current in the s-domain can be expressed as follows:

$$\begin{aligned} \frac{i_L(s)}{v_C(s)} &= \frac{f_s}{s}\frac{V_{\rm in}}{L_s}\frac{1}{S_f + S_{en}}\frac{G_{\rm mLg}R_{\rm eq}}{1+sC_{\rm RP}R_{\rm eq}} \\ &\times \frac{\left(1 - e^{-sT_{\rm on}}\right)\left(1 - e^{-sT_{\rm sw}}\right)}{\left(1 + \frac{S_f}{S_f+S_{en}}\frac{T_{\rm off}}{2R_{Co}C}\right) - \left(1 - \frac{S_f}{S_f+S_{en}}\frac{2T_{\rm on}+T_{\rm off}}{2R_{Co}C_o}\right)e^{-sT_{\rm sw}}}. \end{aligned} \tag{25}$$

With control to the inductor current transfer function, the control to output voltage transfer function can be derived as follows:

$$\begin{aligned} \frac{v_o(s)}{v_C(s)} &= \frac{v_o(s)}{i_L(s)}\frac{i_L(s)}{v_C(s)} \\ &= \frac{R_{Co}Cs+1}{Cs}\frac{f_s}{s}\frac{V_{\rm in}}{L_s}\frac{1}{S_f + S_{en}}\frac{G_{\rm mLg}R_{\rm eq}}{1+sC_{\rm RP}R_{\rm eq}} \\ &\times \frac{\left(1 - e^{-sT_{\rm on}}\right)\left(1 - e^{-sT_{\rm sw}}\right)}{\left(1 + \frac{S_f}{S_f+S_{en}}\frac{T_{\rm off}}{2R_{Co}C}\right) - \left(1 - \frac{S_f}{S_f+S_{en}}\frac{2T_{\rm on}+T_{\rm off}}{2R_{Co}C_o}\right)e^{-sT_{\rm sw}}}. \end{aligned} \tag{26}$$

Based on the Padé approximation, (26) can be further simplified and pole/zero locations can be separated. The approximation is expressed as follows:

$$\frac{v_o(s)}{v_C(s)} \approx \frac{G_{\rm mLg}R_{\rm eq}}{1+sC_{\rm RP}R_{\rm eq}}\frac{R_{Co}Cs+1}{1 + \frac{s}{Q_1\omega_1} + \frac{s^2}{\omega_1^2}}\frac{1}{1 + \frac{s}{Q_2\omega_2} + \frac{s^2}{\omega_2^2}} \tag{27}$$

$$\begin{aligned} &s_f\Delta T_{{\rm off}(i)} + \frac{V_o}{L_sC_o}\left[(T_{\rm on}+T_{\rm off})\sum_{k=1}^{i-1}\Delta t_{{\rm off}(k)} + \frac{T_{\rm off}}{2}\Delta T_{{\rm off}(i)}\right] + S_{en}\Delta T_{{\rm off}(i)} \\ &= \frac{-G_{\rm mLG}R_{\rm eq}\hat{r}}{(2\pi f_m)C_{\rm RP}^2R_{\rm eq}^2 + 1}\sin(\pi f_m(T_{\rm on}+T_{\rm off}))\begin{bmatrix} 2\cos\left(2\pi f_m\left[(i+1)(T_{\rm on}+T_{\rm off}) - \frac{T_{\rm on}-T_{\rm off}}{2}\right] - \theta\right) \\ -4\pi f_m C_{\rm RP}R_{\rm eq}\sin\left(2\pi f_m\left[(i+1)(T_{\rm on}+T_{\rm off}) - \frac{T_{\rm on}-T_{\rm off}}{2}\right] - \theta\right)\end{bmatrix} \end{aligned} \tag{21}$$

where

$$\omega_1 = \pi/T_{\rm on}\ ,\ \ Q_1 = 2/\pi\ ,\ \ \omega_2 = \ \pi/T_{\rm sw}$$

$$Q_2 = \frac{T_{\rm sw}}{\pi\left[\left(1+\frac{s_{en}}{s_f}\right)R_{C_o}C_o - T_{\rm on}/2\right]}$$

$$s_{en} = \frac{G_{\rm mRP}V_{\rm rsc}D}{C_{RP}}\ ,\quad s_f\ = \frac{v_{\rm in}D}{L_s}$$

$$R_{\rm eq} = \frac{V_{\rm ref}}{G_{\rm mRP}V_{\rm rsc}D}.$$

ACKNOWLEDGMENT

The authors would like to thank SIMPLIS Technologies Corporation, USA, for providing the SIMPLIS simulation tool.

REFERENCES

[1] T. Qian and W. Wu, "Analysis of the ramp compensation approaches to improve stability for buck converters with constant on-time control," *IET Power Electron.*, vol. 5, no. 2, pp. 196–204, Feb. 2012.

[2] J. Li and F. C. Lee, "Modeling of V^2 current-mode control," *IEEE Tran. Circuits Syst. I, Reg. Papers*, vol. 57, no. 9, pp. 2552–2563, Sep. 2010.

[3] S. Tian, F. C. Lee, P. Mattavelli, K.-Y. Cheng, and Y. Yan, "Small-signal analysis and optimal design of external ramp for constant on-time V^2 control with multilayer ceramic caps," *IEEE Trans. Power Electron.*, vol. 29, no. 8, pp. 4450–4460, Aug. 2014.

[4] C.-J. Chen, D. Chen, C.-W. Tseng, C.-T. Tseng, Y.-W. Chang, and K. Wang, "A novel ripple-based constant on-time control with virtual inductor current ripple for buck converter with ceramic output capacitors," in *Proc. 26th Annu. IEEE Appl. Power Electron. Conf. Expo.*, Mar. 2011, pp. 1488–1493.

[5] Y.-C. Lin, C.-J. Chen, D. Chen, and B. Wang, "A ripple-based constant on-time control with virtual inductor current and offset cancellation for DC power converters," *IEEE Trans. Power Electron.*, vol. 27, no. 10, pp. 4301–4310, Oct. 2012.

[6] I.-C. Wei, Y.-C. Lin, C.-J. Chen, and D. Chen, "Stability issues and modelling of ripple-based constant on-time control schemes operating in discontinuous conduction mode," *IET Power Electron.*, vol. 7, no. 4, pp. 868–875, Apr. 2014.

[7] Y. Yan, P-H. Liu, F. C. Lee, Q. Li, and S. Tian, "V^2 control with capacitor current ramp compensation using lossless capacitor current sensing," in *Proc. Energy Convers. Congr. Expo.*, Sep. 2013, pp. 117–124.

[8] Texas Instruments, "Single phase D-CAP + TM mode step down controller for IMVP6 + CPU/GPU Vcore TPS51610 datasheet," 2009. [Online]. Available: http://www.ti.com/product/tps51610

[9] L. Kong, D. Chen, S.-F. Hsiao, C.-F. Nieu, C.-J. Chen, and K.-F. Li, "A novel adaptive-ramp ripple-based constant on-time buck converter for stability and transient optimization in wide operation range," *IEEE J. Emerg. Sel. Topics Power Electron.*, vol. 6, no. 3, pp. 1314–1324, Sep. 2018.

[10] J. Li and F. C. Lee, "New modeling approach and equivalent circuit representation for current-mode control," *IEEE Trans. Power Electron.*, vol. 25, no. 5, pp. 1218–1230, May 2010.

[11] Richtek Corp, "Advanced constant-on time synchronous step-down converters," 2015. [Online]. Available: https://www.richtek.com/∼/media/AN%20PDF/SG002_EN.pdf

[12] Texas Instruments, "Guidelines for choosing the right buck regulator control strategy—Part B," 2015. [Online]. Available: http://edu.21ic.com/uploads/down/edu/2015/1447033785_9316.pdf

[13] S. Tian, F. C. Lee, Q. Li, and Y. Yan, "Unified equivalent circuit model of V^2 control," in *Proc. IEEE Appl. Power Electron. Conf. Expo.*, 2014, pp. 1016–1023.

[14] Y. Yan, F. C. Lee, P. Mattavelli, and S. Tian, "Small signal analysis of V^2 control using equivalent circuit model of current mode controls," *IEEE Trans. Power Electron.*, vol. 31, no. 7, pp. 5344–5353, Jul. 2016.

[15] T. Qian, "Subharmonic analysis for buck converters with constant on-time control and ramp compensation," *IEEE Trans. Ind. Electron.*, vol. 60, no. 5, pp. 1780–1786, May 2013.

[16] C.-C. Fang and R. Redl, "Subharmonic stability limits for the buck converter with ripple-based constant on-time control and feedback filter," *IEEE Trans. Power Electron.*, vol. 29, no. 4, pp. 2135–2142, Apr. 2014.

[17] Texas Instruments, "TPS65094x PMIC for Intel™ Apollo lake platform datasheet," 2017. [Online]. Available: http://www.ti.com/lit/ds/swcs133b/swcs133b.pdf

[18] C.-F. Nien *et al.*, "A novel adaptive quasi-constant on-time current-mode buck converter," *IEEE Trans. Power Electron.*, vol. 32, no. 10, pp. 8124–8133, Oct. 2017.

Wen-Chin Liu was born in Hualien, Taiwan. He received the B.S. degree in electronic and computer engineering from the National Taiwan University of Science and Technology, Taipei, Taiwan, in 2017, and the M.S. degree in electrical engineering from National Taiwan University, Taipei in 2019. He is currently working toward the Ph.D. degree in electrical and computer engineering with the University of California San Diego, San Diego, CA, USA.

His current research interests include modeling, analysis, and control strategies of dc–dc power converters for point-of-load applications, high-frequency high-power-density dc–dc resonant converters, power integrated circuits, and the power management of integrated circuits.

Ching-Jan Chen (S'08–M'12–SM'18) received the B.S. and Ph.D. degrees in electrical engineering from National Taiwan University, Taipei, Taiwan, in 2006 and 2011, respectively.

From 2010 to 2011, he was a Visiting Scholar with the Center of Power Electronic Systems, Virginia Tech, Blacksburg, VA, USA. From 2011 to 2015, he was a Senior Engineer with the Department of IC Research and Development, Richtek Technology Corporation, Hsinchu, Taiwan. Since 2015, he has been an Assistant Professor with the Department of Electrical Engineering, National Taiwan University. His current research interests include modeling and control of dc–dc and ac–dc power converters, power conversion for CPU and mobile devices, and power IC design.

Ching-Hsiang Cheng (S'18) was born in Chiayi, Taiwan. He received the B.S. degree in electrical engineering from the National Yunlin University of Science and Technology, Yunlin, Taiwan, in 2010, and the M.S. degree in electrical engineering from National Tsing Hua University, Hsinchu, Taiwan, in 2012. He is currently working toward the Ph.D. degree with the Department of Electrical Engineering, National Taiwan University, Taipei, Taiwan.

Since 2012, he has been an Engineer with the Center of System Development, Richtek Technology Corporation, Hsinchu, where his work focuses on the system analysis and design of controller for ac–dc charger. His current research interests include modeling, analysis, and control of ac–dc and dc–dc power converters, power integrated circuits, smart power management integrated circuits, and thermal evaluation for monolithic power integrated circuits.

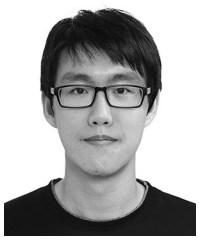

Hsuan-Ju Chen was born in Kaohsiung, Taiwan, in 1990. He received the B.S. and M.S. degrees in electrical engineering from National Cheng Kung University, Tainan, Taiwan, in 2012 and 2014, respectively.

Since 2015, he has been a Design Engineer with Richtek Corporation, Hsinchu, Taiwan. His research interests include power management and analog integrated circuit design.